

A Large Scale Cosserat Point Contact/Impact Formulation Using Object – Oriented Programming

GJ. Lo¹, P. Papadopoulos^{1**}

¹Department of Mechanical Engineering, University of California, Berkeley, CA 94720-1740, USA

Abstract

This article discusses a discrete element method that employs the theory of non-linearly elastic Cosserat points. The method is applied to frictionless multi-body contact between ellipsoids. Time integration and the detection and treatment of contacts are discussed in connection with the computer implementation of the method.

Keywords: Discrete element method, contact, impact, Cosserat point.

Introduction

Numerous problems of interest in science and engineering involve the dynamic interactions between large numbers of geometrically similar bodies, such as powders, grains, rocks, etc. Representative applications include hopper flows in the food and pharmaceutical industries, soil and rock stability in geomechanics, and planetesimal formation in astrophysics. In many cases, the motions of interacting particles cannot be accurately modeled as rigid. This is especially true when one is interested in long-term dynamics, where the presence of even small amounts of strain energy is sufficient to significantly alter the overall system response. On the other hand, owing to the complexity of the problem, it is often computationally intractable to treat each particle as a general deformable continuum. This paper employs the theory of Cosserat points, which constitutes a compromise between the extreme modeling choices of rigid and fully deformable continua. A three-dimensional Cosserat point consists of a point in three-dimensional Euclidean space and a set of three-dimensional vectors called directors attached to that point. The directors “carry” information about the deformation of a three-dimensional continuum associated with the Cosserat point. The theory of Cosserat points was proposed by Rubin [1] and Green and Naghdi [2], who extended Rubin's original work from 3 to K directors. The Cosserat point theory is methodologically motivated by the director theories of rods and shells, see, *e.g.*, [3,4]. However, it traces its conceptual origins in the discrete elasticity theory of Wozniak [5,6] and the theory of homogeneously deforming continua by Slawianowski [7,8]. A similar theory, albeit approached from a somewhat different viewpoint, is advocated by Cohen and Muncaster under the “pseudo-rigid” body formalism, see [9] for a comprehensive review.

** Corresponding author

The Cosserat point theory has been already employed to model single bodies [10], small collections of disconnected bodies [11], and connected multi-bodies [12]. In this paper, this theory is put to use in modeling large-scale frictionless particle interactions in a dynamic setting. The paper places emphasis on modeling, as well as on the application of algorithms to detect and treat collisions in a mathematically consistent and computationally efficient manner. The main objective of the paper is to illustrate the applicability of the theory to particle simulations and lay the groundwork for its use in assessing the significance of particle deformation in the long-term dynamics of particulate flows.

The organization of the paper is as follows: Section 2 includes a brief, self-contained introduction to the theory of a Cosserat point, and describes a simple elastic model used in the subsequent simulations. Contact between Cosserat points with ellipsoidal configurations is treated in Section 3, and is followed by a short description of the adaptive time-integration method in Section 4. Selected numerical simulations are presented in Section 5, followed by a short conclusion section.

1. Theory of elastic Cosserat points

1.1 General equations

Consider a body \mathcal{B} which, at a given time t_0 , occupies a region \mathfrak{R}_0 with smooth boundary $\partial\mathfrak{R}_0$ in the Euclidean point space \mathcal{E}^3 . The same body occupies at time t a region \mathfrak{R} having smooth boundary $\partial\mathfrak{R}$. The regions \mathfrak{R}_0 and \mathfrak{R} constitute the reference and present configuration of the body, respectively. A material point X in the body can be identified by convected coordinates X^i ($i = 1, 2, 3$). Without any loss of generality, these coordinates are assumed Cartesian in the reference configuration relative to a fixed orthonormal basis $\{\mathbf{E}_1, \mathbf{E}_2, \mathbf{E}_3\}$.

Let the position vector of a material point X in the body be denoted in the present configuration by \mathbf{r}^* and be written as

$$\mathbf{r}(X^i, t) = \mathbf{r}(t) + \lambda^N(X^i)_N \mathbf{d}(t) \quad (1)$$

Here, \mathbf{r} is the position vector of the Cosserat point, while \mathbf{d}_N and λ^N , $N = 1, \dots, K$, are the directors and the associated weights, respectively. Note that the usual summation convention applies to repeated indices, unless stated otherwise. Equation (1) specifies the motion of the Cosserat continuum in terms of the motion of the Cosserat point and the change in magnitude and orientation of the directors. In direct analogy to (1), and upon denoting respectively by \mathbf{r}_0^* , \mathbf{r}_0 and \mathbf{D}_N , $N = 1, \dots, K$, the position vector of the material point X , the position vector of the Cosserat point, and the directors in the reference configuration, write

$$\mathbf{r}_0^*(X^i) = \mathbf{r}_0 + \lambda^N(X^i)_N \mathbf{D}_N \quad (2)$$

The velocity and director velocities of the Cosserat point are defined as

$$\mathbf{w} = \dot{\mathbf{r}} \quad , \quad \mathbf{w}_N = \dot{\mathbf{d}}_N \quad , \quad N = 1, \dots, K \quad (3)$$

where a superposed dot denotes material time derivative.

Following the work of Rubin [1] and Green and Naghdi [2], define the total mass m and the inertia coefficients y^N and y^{NM} , $N, M = 1, \dots, K$ of the Cosserat point as

$$\begin{aligned} m &= \int_{\mathfrak{B}_0} \rho_0 dV, \\ my^N &= \int_{\mathfrak{B}_0} \rho_0 \lambda^N dV, \\ my^{NM} &= \int_{\mathfrak{B}_0} \rho_0 \lambda^N \lambda^M dV \end{aligned} \quad (4)$$

where $\rho_0 = \hat{\rho}_0(X^i)$ is the mass density in the reference configuration. In addition, define the total applied force \mathbf{f} and the total applied director forces \mathbf{I}^N , $N = 1, \dots, K$, as

$$\begin{aligned} \mathbf{f} &= \int_{\partial\mathfrak{B}_0} \mathbf{p} dA + \int_{\mathfrak{B}_0} \rho_0 \mathbf{b} dV, \\ \mathbf{I}^N &= \int_{\partial\mathfrak{B}_0} \lambda^N \mathbf{p} dA + \int_{\mathfrak{B}_0} \rho_0 \lambda^N \mathbf{b} dV \end{aligned} \quad (5)$$

in terms of the body force \mathbf{b} per unit mass and the contact tractions \mathbf{p} per unit referential area.

Taking into account (4), conservation of mass in a Cosserat point can be expressed as

$$\dot{m} = 0, \quad \dot{y}^N = 0, \quad \dot{y}^{NM} = 0, \quad N, M = 1, \dots, K \quad (6)$$

Likewise, with reference to (5), linear momentum balance and director momentum balance are written as

$$\begin{aligned} m(\dot{\mathbf{v}} + y^N \dot{\mathbf{w}}_N) &= \mathbf{f}, \\ m(y^N \dot{\mathbf{v}} + y^{NM} \dot{\mathbf{w}}_N) &= \mathbf{I}^N - \mathbf{k}^N, \quad N = 1, \dots, K \end{aligned} \quad (7)$$

respectively, while angular momentum balance takes the form

$$\mathbf{d}_N \times \mathbf{k}^N = 0 \quad (8)$$

In equations (7) and (8), \mathbf{k}^N , $N = 1, \dots, K$, are the intrinsic director forces which can be regarded as direct counterparts of the stress tensor in classical continuum mechanics.

In the theory of a Cosserat point, the intrinsic director forces require constitutive prescription. Assuming that the Cosserat point is made of a Green-elastic material, the strain energy ψ per unit mass should, in principle, depend on \mathbf{d}_N and \mathbf{D}_N , $N = 1, \dots, K$. However, invariance requirements necessitate that the strain energy be expressed as a function

$$\psi = \hat{\psi}(\mathbf{d}_N \cdot \mathbf{d}_M, \mathbf{D}_N \cdot \mathbf{D}_M), \quad N, M = 1, \dots, K \quad (9)$$

see [13]. Furthermore, work-conjugacy between \mathbf{k}^N and \mathbf{d}_N implies that

$$\mathbf{k}^N = m \frac{\partial \hat{\psi}}{\partial \mathbf{d}_N} \quad (10)$$

Note that, since $\frac{\partial \hat{\psi}}{\partial \mathbf{d}_N}$ is parallel to \mathbf{d}_N due to the form the strain energy function in (9), the angular momentum equation (8) is satisfied identically for any Green-elastic Cosserat point.

1.2 A simple Cosserat point model

The purpose of this section is to describe in detail a specific Cosserat point model that is subsequently employed in the numerical simulation of deformable particles. To this end, let each Cosserat point be endowed with three directors ($K = 3$) and let the weighting functions in (1) and (2) be given by

$$\lambda^N = X^N, \quad N = 1, 2, 3 \quad (11)$$

Also, choose the origin of the fixed orthonormal basis $\{\mathbf{E}_1, \mathbf{E}_2, \mathbf{E}_3\}$ to coincide with the mass center of the body in the reference configuration and take \mathbf{E}_N , $N = 1, 2, 3$ to be parallel to the body's principal axes of inertia. In addition, without loss of generality, let the directors in the reference configuration coincide with the basis vectors, namely

$$\mathbf{D}_N = \mathbf{E}_N, \quad N = 1, 2, 3 \quad (12)$$

Under the preceding assumptions, equations (1) and (2) imply that the deformation gradient \mathbf{F} , defined by the relation $d\mathbf{r}^* = \mathbf{F}d\mathbf{r}_0^*$, takes the simple form

$$\mathbf{F} = \mathbf{d}_N \otimes \mathbf{E}^N \quad (13)$$

where “ \otimes ” denotes tensor product, and $\mathbf{E}^N = \delta^{NM} \mathbf{E}_M$, $N = 1, 2, 3$, with δ^{NM} being the Kronecker delta. Throughout this work, it is assumed that the three directors \mathbf{d}_N deform in such a manner that $\det \mathbf{F} > 0$. Upon further assuming that \mathbf{r} in (1) is the position vector of the mass center of the body under consideration, it follows from (1), (2) and (13) that

$$\boldsymbol{\pi} = \mathbf{F}\boldsymbol{\Pi} \quad (14)$$

where $\boldsymbol{\pi} = \mathbf{r}^* - \mathbf{r}$ and $\boldsymbol{\Pi} = \mathbf{r}_0^* - \mathbf{r}_0$ are the relative position vectors of particle X in the present and reference configurations, respectively. Equation (13) implies that the deformation in this Cosserat point model is spatially homogeneous (*i.e.*, it is the same for all particles). Taking into account (13) it is readily shown that the Lagrangian strain, defined by $\mathbf{E} = \frac{1}{2}(\mathbf{F}^T \mathbf{F} - \mathbf{I})$, where \mathbf{I} is the second-order identity tensor, can be expressed as

$$\mathbf{E} = \frac{1}{2}(\mathbf{d}_N \cdot \mathbf{d}_M - \delta_{NM}) \mathbf{E}^N \otimes \mathbf{E}^M \quad (15)$$

In this model, the Cosserat point is made of a homogeneous isotropic Kirchhoff-St. Venant material, which, for fully-deformable continua, is associated to the strain energy

$$\psi^* = \bar{\psi}^*(\mathbf{E}) = \frac{1}{2\rho_0} \left[\lambda (\text{tr} \mathbf{E})^2 + 2\mu \mathbf{E} \cdot \mathbf{E} \right] \quad (16)$$

where λ and μ are material constants. Note that, in the Cosserat continuum, \mathbf{E} (hence also ψ^*) is a function of time only, which, with the aid of (15) and (16), implies that the total strain energy of the Cosserat point is given by

$$m\psi = V\rho_0\psi^* = \frac{V}{2} \left[\frac{\lambda}{4} (\mathbf{d}_N \cdot \delta^{NM} \mathbf{d}_M - 3)^2 + \right. \\ \left. + \frac{\mu}{2} \left\{ (\mathbf{d}_N \cdot \delta^{NK} \mathbf{d}_M) (\mathbf{d}_K \cdot \delta^{LM} \mathbf{d}_L) - 2\mathbf{d}_N \cdot \delta^{NM} \mathbf{d}_M + 3 \right\} \right] \quad (17)$$

where V is the total volume of the body in the present configuration. Appealing to (10) and (17), the intrinsic director force now takes the form

$$\mathbf{k}^N = \frac{V}{2} \left[\lambda (\mathbf{d}_K \cdot \delta^{KM} \mathbf{d}_M - 3) \delta^{NL} \mathbf{d}_L + 2\mu \left\{ (\mathbf{d}_K \cdot \delta^{LM} \mathbf{d}_L) \delta^{NK} - \delta^{NM} \right\} \mathbf{d}_M \right] \quad (18)$$

Recalling (11) and that the origin of $\{\mathbf{E}_N\}$ coincides with the mass center of the body, it follows readily that the inertia coefficients y^N in (4)₂ vanish identically. Consequently, the equations of linear momentum balance in (7)₁ and director momentum balance in (7)₂ reduce to

$$m\dot{\mathbf{v}} = \mathbf{f}, \\ my^{NM} \dot{\mathbf{w}}_N = \mathbf{I}^N - \boldsymbol{\kappa}^N, \quad N = 1, \dots, K \quad (19)$$

Furthermore, given (4)₃ and (11), the inertia coefficients y^{NM} in (19)₂ can be expressed as

$$my^{NM} = \int_0 \rho_0 X^N X^M dV, \quad N, M = 1, 2, 3 \quad (20)$$

Since the basis vectors \mathbf{E}_N , $N = 1, 2, 3$ are chosen to lie along the principal axis of the inertia tensor, it trivially follows that $my^{NN} = 0$, $N = 1, 2, 3$, (no sum on N).

In the problem at hand, the applied forces are due to gravity (equal, by convention to $-\mathbf{g}$ per unit mass) and direct contact between the particles, while the applied director forces vanish identically. Neglecting, for now, the contact forces, this implies that

$$\mathbf{f} = -m(\mathbf{g} \cdot \mathbf{E}^N) \mathbf{E}_N = -mg^N \mathbf{E}_N, \quad \mathbf{I}^N = 0 \quad (21)$$

The effect of the contact forces is discussed in detail in Section 3.3.

For the sake of clarity, write the components of \mathbf{r} , \mathbf{d}_N , \mathbf{w}_N and \mathbf{k}^N relative to the bases $\{\mathbf{E}_N\}$ and $\{\mathbf{E}^N\}$ as

$$r_N = \mathbf{r} \cdot \mathbf{E}_N, \quad d_{NM} = \mathbf{d}_N \cdot \mathbf{E}_M, \quad w_{NM} = \mathbf{w}_N \cdot \mathbf{E}_M, \quad k_M^N = \mathbf{k}^N \cdot \mathbf{E}_M \quad (22)$$

where $N, M = 1, 2, 3$. Now, introduce the vectors \mathbf{z}_1 , \mathbf{z}_2 , \mathbf{k} and \mathbf{q} containing the components of the generalized position, velocity, intrinsic force, and applied force, respectively, as

$$\begin{aligned} [\mathbf{z}_1] &= [r_1 \ r_2 \ r_3 \ d_{11} \ d_{12} \ d_{13} \ d_{21} \ d_{22} \ d_{23} \ d_{31} \ d_{32} \ d_{33}]^T, \\ [\mathbf{z}_2] &= [v_1 \ v_2 \ v_3 \ w_{11} \ w_{12} \ w_{13} \ w_{21} \ w_{22} \ w_{23} \ w_{31} \ w_{32} \ w_{33}]^T, \\ [\mathbf{k}] &= [0 \ 0 \ 0 \ k_1^1 \ k_2^1 \ k_3^1 \ k_1^2 \ k_2^2 \ k_3^2 \ k_1^3 \ k_2^3 \ k_3^3]^T, \\ [\mathbf{q}] &= [-mg^1 \ -mg^2 \ -mg^3 \ 0 \ 0 \ 0 \ 0 \ 0 \ 0 \ 0 \ 0 \ 0]^T. \end{aligned} \quad (23)$$

The momentum equations (19) can now be written compactly in first-order form as

$$\begin{aligned}\dot{\mathbf{z}}_1 &= \mathbf{z}_2, \\ \dot{\mathbf{z}}_2 &= \mathbf{M}^{-1}[-\mathbf{k}(\mathbf{z}_1 + \mathbf{q})] = h(\mathbf{z}_1)\end{aligned}\quad (24)$$

where the generalized inertia matrix \mathbf{M} is given by

$$[\mathbf{M}] = \begin{bmatrix} m[I] & [0] & [0] & [0] \\ [0] & my^{11}[I] & [0] & [0] \\ [0] & [0] & my^{22}[I] & [0] \\ [0] & [0] & [0] & my^{33}[I] \end{bmatrix}\quad (25)$$

In equation (25), $[I]$ and $[0]$ denote 3×3 identity and zero submatrices, respectively.

2. Contact between Cosserat points

This section outlines an efficient and robust treatment of contact between elastic Cosserat points occupying ellipsoidal configurations. Specifically, it describes a method of contact detection, as well as a sorting technique for reducing the computational cost of tracking contact between such Cosserat points.

Many solid objects can be accurately approximated as quadric-surface bodies, such as spheres, ellipsoids, elliptic cylinders, etc. This geometric approximation has been employed extensively in modeling granular systems [14-16], rocks [17], particle packing problems [18] and computer-aided design [19]. In this work, attention is focused specifically on (triaxial) ellipsoids, whose surface can be mathematically represented as

$$\boldsymbol{\rho} = a^1 \cos(u) \cos(v) \mathbf{E}_1 + a^2 \cos(u) \sin(v) \mathbf{E}_2 + a^3 \sin(u) \mathbf{E}_3\quad (26)$$

Here, $\boldsymbol{\rho}$ is the position vector of a surface point measured from the center of the ellipsoid, a^N , $N = 1, 2, 3$, are the lengths of the principal semi-axes and \mathbf{E}_N , $N = 1, 2, 3$, are the unit vectors parallel to the principal directions of the ellipsoid¹. Also, the parameters $u \in [-\pi/2, \pi/2]$ and $v \in [0, 2\pi)$ are curvilinear surface coordinates corresponding to the polar and azimuthal angle, respectively.

The choice of ellipsoids is guided by the observation that they are geometrically invariant under the homogeneous deformation associated with the Cosserat point model. Said differently, ellipsoids are always mapped to ellipsoids by the action of a spatially homogeneous deformation gradient $\mathbf{F}(t)$, see [20, Section 27]. This result can be easily deduced by representing an ellipsoidal surface in the reference configuration as

$$\boldsymbol{\Pi} \cdot \mathbf{K} \boldsymbol{\Pi} = 1\quad (27)$$

where \mathbf{K} is, by assumption, positive-definite. Then, upon recalling (14), it follows that

$$\boldsymbol{\pi} \cdot (\mathbf{F}^{-T} \mathbf{K} \mathbf{F}^{-1}) \boldsymbol{\pi} = 1\quad (28)$$

¹ The principal directions of the ellipsoid coincide with the principal directions of the inertial tensor, assuming, as is done here, that the body is homogeneous

Noting that $\mathbf{F}^{-T}\mathbf{K}\mathbf{F}^{-1}$ is also positive-definite, equation (28) represents an ellipsoid in the current configuration with principal directions oriented along the eigenvectors of $\mathbf{F}^{-T}\mathbf{K}\mathbf{F}^{-1}$.

2.1 Sorting of contact pairs

Consider the problem of contact between two Cosserat points embedded in \mathcal{E}^3 . Equation (27) implies that the boundary of each body in the reference configuration can be determined the position vectors $\mathbf{r}_0^{(\alpha)}$ of the mass centers and by the tensors $\mathbf{K}^{(\alpha)}$, $\alpha = 1, 2$. Then, the respective boundaries in the current configuration can be determined from the position vectors \mathbf{r}_α and the directors $\mathbf{d}_N^{(\alpha)}$. This section discusses a low-cost, two-stage sorting procedure intended to avoid a costly all-to-all contact detection check by substantially reducing the number of potential contact pairs. This procedure consists of a spatial sorting stage, followed by a spherical sorting stage. Generally, spatial sorting is more efficient than spherical sorting. However, spherical sorting can yield additional restrictions to the feasible set of contact pairs. Hence, the two methods are employed in sequence. Although the forthcoming analysis can be extended to contact between general convex regions in \mathcal{E}^3 , the discussion focuses specifically on ellipsoids. An application to the case of contact between superquadric ellipsoids can be found in [21].

Generally, the choice of an optimal sorting procedure is strongly dependent on the problem at hand. Several sorting algorithms are classified and discussed in [22] for different types of problems. Here, an efficient spatial sorting algorithm is adopted following earlier work by Munjiza and Andrews [14]. This is well-suited for dynamic problems including loose and/or dense packing of objects. Its principal limitation, which is of minor significance in this work, is that it applies to systems of similarly sized bodies. The algorithm is based on decomposition of the ambient three-dimensional space into identical cubic cells of size $2r_0 \times 2r_0 \times 2r_0$, where r_0 is the maximum over the lengths of the semi-axes of all ellipsoids in the reference configuration. Each ellipsoid is assigned an integer identification $1, 2, \dots, n$, where n is the total number of ellipsoids. In a similar fashion, each cubic cell is assigned an integer triad identification (ix, iy, iz) .

A mapping between the set of all ellipsoids and the cubic cells is effected at any solution time by assigning each ellipsoid to one and only one cell. For instance, an ellipsoid whose mass center has coordinates (x, y, z) relative to the orthonormal basis $\{\mathbf{E}_N\}$ is assigned to the cell (ix, iy, iz) , such that

$$ix = \text{Int}\left(\frac{x - x_0}{2r_0}\right), \quad iy = \text{Int}\left(\frac{y - y_0}{2r_0}\right), \quad iz = \text{Int}\left(\frac{z - z_0}{2r_0}\right) \quad (29)$$

where (x_0, y_0, z_0) are the coordinates of the origin of a reference point (typically a vertex of the block comprised by the cubic cells), see also Section 4, while “Int” is the standard integer truncation operator. Once all ellipsoids are mapped to cells, detection of potential contact for any given ellipsoid only needs to involve ellipsoids mapped to immediately neighboring cells.

Spherical sorting is performed at any solution time by comparing the Euclidean distance $R^{(\alpha\beta)} = \|\mathbf{r}^{(\beta)} - \mathbf{r}^{(\alpha)}\|$ between the current mass centers of two ellipsoids identified by α and β ($\alpha \neq \beta$) to the sum of the lengths of their largest principal semi-axes $R^{(\alpha)}$ and $R^{(\beta)}$, see Fig. (1). Clearly, the condition

$$R^{(\alpha\beta)} > R^{(\alpha)} + R^{(\beta)} \tag{30}$$

would eliminate the pair (α, β) of ellipsoids from further contact consideration.

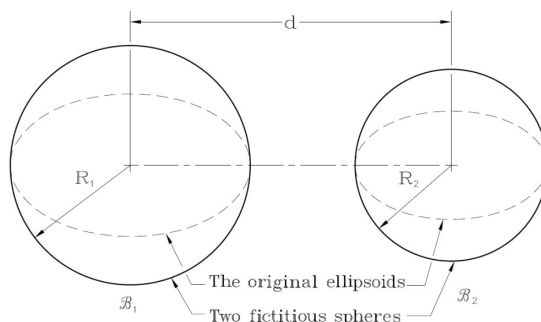


Fig. 1. The detection of potential contact.

2.2 Contact detection

The second step in contact detection applies to all candidate pairs (α, β) of ellipsoids obtained by the sorting processes. For such pairs, write the non-negative distance function $d^{(\alpha\beta)}$ between any two surface points with curvilinear surface coordinates $(u^{(\alpha)}, v^{(\alpha)})$ and $(u^{(\beta)}, v^{(\beta)})$ as

$$d^{(\alpha\beta)} = \hat{d}^{(\alpha\beta)}(u^{(\alpha)}, v^{(\alpha)}, u^{(\beta)}, v^{(\beta)}) = \|\bar{\mathbf{r}}^{(\beta)} - \bar{\mathbf{r}}^{(\alpha)}\| \tag{31}$$

where $\bar{\mathbf{r}}^{(\alpha)}$ denotes the position vector of the point on the boundary of body α in the present configuration. The goal is to determine two points, labeled $P^{(\alpha)}$ and $P^{(\beta)}$, on the two ellipsoidal surfaces for which $d^{(\alpha\beta)}$ attains a global minimum. Upon considering Fig. 2, it is immediately clear that it is not always possible to find a *unique* pair of such points when the bodies have already penetrated each other. Indeed, in this case all pairs of points on the intersection curve generated by the overlapping ellipsoids yield $d^{(\alpha\beta)} = 0$. The discussion of this case is postponed until the end of this section.

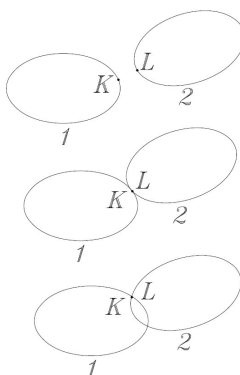


Fig. 2. The contact situations between two ellipsoidal bodies.

A simple algorithm is proposed here to determine a (unique) pair $(P^{(\alpha)}, P^{(\beta)})$ of points on the two ellipsoids that minimizes the distance function $d^{(\alpha\beta)}$ when there is no penetration. The algorithm starts by arbitrarily selecting a pair of points $(P_1^{(\alpha)}, P_1^{(\beta)})$ on the respective surfaces, see Fig. (3). Then, keeping $P_1^{(\alpha)}$ fixed, a new point $P_2^{(\beta)}$ is determined on ellipsoid β which minimizes $d^{(\alpha\beta)}$ with respect to variables $(u^{(\beta)}, v^{(\beta)})$. Subsequently, keeping $P_2^{(\beta)}$ fixed, a point $P_1^{(\alpha)}$ is determined on ellipsoid α which again minimizes $d^{(\alpha\beta)}$ with respect to variables $(u^{(\alpha)}, v^{(\alpha)})$, and so forth. Note that each iteration yields a unique minimum corresponding to the distance of a point from a convex set, see, *e.g.*, [23]. This multivariate cyclic descent method produces a sequence of points on the two surfaces that can be shown to converge to the pair $(P^{(\alpha)}, P^{(\beta)})$, see, *e.g.*, [24]. A standard variable metric method (BFGS) is employed to solve the local minimization problems, see [25]. Upon determining the pair $(P^{(\alpha)}, P^{(\beta)})$, the associated outward surface normal vectors $\mathbf{n}^{(\alpha)}$ and $\mathbf{n}^{(\beta)}$ to the ellipsoids at these points must be equal and opposite, provided that the ellipsoids are not in contact with each other. Indeed, in such case the extremization of $\hat{d}^{(\alpha\beta)}$ in (31) leads to

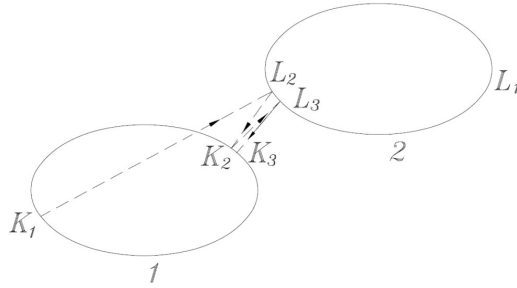


Fig. 3. From initial guesses K_1 and L_1 , a sequence of points L_2, K_2, L_3, \dots is calculated which minimizes the distance function d defined in equation (31).

$$\frac{\bar{\mathbf{r}}^{(\alpha)} - \bar{\mathbf{r}}^{(\beta)}}{\|\bar{\mathbf{r}}^{(\alpha)} - \bar{\mathbf{r}}^{(\beta)}\|} \cdot \frac{\partial \bar{\mathbf{r}}^{(\alpha)}}{\partial u^{(\alpha)}} = 0 \quad , \quad \frac{\bar{\mathbf{r}}^{(\alpha)} - \bar{\mathbf{r}}^{(\beta)}}{\|\bar{\mathbf{r}}^{(\alpha)} - \bar{\mathbf{r}}^{(\beta)}\|} \cdot \frac{\partial \bar{\mathbf{r}}^{(\alpha)}}{\partial v^{(\alpha)}} = 0 \quad (32)$$

and

$$\frac{\bar{\mathbf{r}}^{(\alpha)} - \bar{\mathbf{r}}^{(\beta)}}{\|\bar{\mathbf{r}}^{(\alpha)} - \bar{\mathbf{r}}^{(\beta)}\|} \cdot \frac{\partial \bar{\mathbf{r}}^{(\beta)}}{\partial u^{(\beta)}} = 0 \quad , \quad \frac{\bar{\mathbf{r}}^{(\alpha)} - \bar{\mathbf{r}}^{(\beta)}}{\|\bar{\mathbf{r}}^{(\alpha)} - \bar{\mathbf{r}}^{(\beta)}\|} \cdot \frac{\partial \bar{\mathbf{r}}^{(\beta)}}{\partial v^{(\beta)}} = 0 \quad (33)$$

Since the ellipsoids do not overlap, equations (32) and (33) imply that the vector $\bar{\mathbf{r}}^{(\alpha)} - \bar{\mathbf{r}}^{(\beta)}$ is perpendicular to the tangent planes of both ellipsoids at points $P^{(\alpha)}$ and $P^{(\beta)}$. In addition, since the ellipsoidal surfaces are orientable, it follows that their outward unit normals at points $P^{(\alpha)}$ and $P^{(\beta)}$ must necessarily be equal and opposite. In summary, denote the position vectors of points $P^{(\alpha)}$ and $P^{(\beta)}$ by $\bar{\mathbf{r}}^{(\alpha)}$ and $\bar{\mathbf{r}}^{(\beta)}$, and the corresponding outward unit normals by $\bar{\mathbf{n}}^{(\alpha)}$

and $\bar{\mathbf{n}}^{(\beta)}$, respectively. Then, the criteria for "no-contact" between two ellipsoids can be expressed as

$$\left(\bar{\mathbf{r}}^{(\alpha)} - \bar{\mathbf{r}}^{(\beta)}\right) \cdot \bar{\mathbf{n}}^{(\alpha)} > 0 \quad , \quad \bar{\mathbf{n}}^{(\alpha)} \cdot \bar{\mathbf{n}}^{(\beta)} = -1 \quad (34)$$

If the criteria in (34) are not met, the ellipsoids are either contacting or penetrating each other. The latter case may occur when the constraint of impenetrability is relaxed by means of a penalty method, as in Section 3.3. When there is penetration, it is essential to identify a unique pair of "contact points" out of the whole set of points that lie on the intersection curve where the constraint forces that ultimately enforce impenetrability are to be applied. A simple, efficient and geometrically unbiased procedure to determine such points is proposed here. To this end, consider two interpenetrating ellipsoids α and β , as in Fig. 4. One may uniformly scale ellipsoid β to obtain a series of fictitious ellipsoids, each having the same orientation as β and principal semi-axes whose lengths are multiplied by a positive scalar τ (≤ 1). As seen from

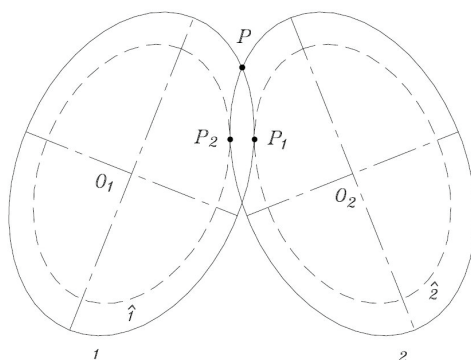


Fig. 4. Unique contact point determination.

Fig. 4, there exists a unique τ , such that the fictitious ellipsoid $\hat{\beta}$ intersects with ellipsoid α at a single point $P^{(\alpha)}$ with position vector $\bar{\mathbf{r}}^{(\alpha)}$ and outward unit normal $\bar{\mathbf{n}}^{(\alpha)}$. This point is now taken to be the unique contact point on the surface of ellipsoid α and is determined by solving the system

$$\bar{\mathbf{r}}^{(\alpha)} = \bar{\mathbf{r}}^{(\hat{\beta})} \quad , \quad \bar{\mathbf{n}}^{(\alpha)} \cdot \bar{\mathbf{n}}^{(\hat{\beta})} = -1 \quad (35)$$

Note that there are five linearly independent equations in (35) and five unknowns, namely $u^{(\alpha)}$, $v^{(\alpha)}$, $u^{(\hat{\beta})}$, $v^{(\hat{\beta})}$, and τ . This system is solved by Newton's method with an initial guess corresponding to any point on the intersection curve of the two ellipsoids. Upon interchanging the roles of α , β and applying the same procedure, one may determine a unique contact point $P^{(\beta)}$ on β , which completes the process.

2.3 Contact constraints and contact forces

When two Cosserat points are in contact, their position vectors and directors are jointly subject by the impenetrability constraint. Here, this constraint is treated in a dual (rather than primal)

manner, namely by introducing Lagrange multipliers under the normality assumption advocated by Casey for the treatment of general constrained continua, [26,27].

To identify a mathematical representation of impenetrability, consider again the points $P^{(\alpha)}$ and $P^{(\beta)}$ at which the ellipsoids α and β are closest to each other, as depicted in Fig. 5. Recalling the discussion in Section 3.2, the distance function $d^{(\alpha\beta)}$ satisfies

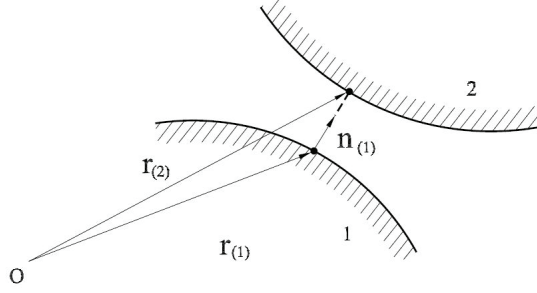


Fig. 5. Schematic depiction of the kinematic quantities involved in describing the contact between two bodies.

$$\begin{aligned}
 d^{(\alpha\beta)} &= \left\| \bar{\mathbf{r}}^{(\beta)} - \bar{\mathbf{r}}^{(\alpha)} \right\| \\
 &= \left(\bar{\mathbf{r}}^{(\beta)} - \bar{\mathbf{r}}^{(\alpha)} \right) \cdot \bar{\mathbf{n}}^{(\alpha)} \\
 &= \left(\mathbf{r}^{(\beta)} + \bar{X}^{(\beta)N} \mathbf{d}_N^{(\beta)} - \mathbf{r}^{(\alpha)} - \bar{X}^{(\alpha)N} \mathbf{d}_N^{(\alpha)} \right) \cdot \bar{\mathbf{n}}^{(\alpha)} \\
 &= \tilde{\phi}_1 \left(\mathbf{z}_1^{(\alpha)}, \mathbf{z}_1^{(\beta)} \right)
 \end{aligned} \tag{36}$$

where use is made of (1), (11) and (23)₁. Likewise, the rate of change of $d^{(\alpha\beta)}$ keeping the material point $P^{(\alpha)}$ fixed can be expressed as

$$\begin{aligned}
 \dot{d}^{(\alpha\beta)} &= \left(\overset{*}{\bar{\mathbf{r}}}^{(\beta)} - \dot{\bar{\mathbf{r}}}^{(\alpha)} \right) \cdot \bar{\mathbf{n}}^{(\alpha)} \\
 &= \tilde{\phi}_2 \left(\mathbf{z}_1^{(\alpha)}, \mathbf{z}_1^{(\beta)}, \mathbf{z}_2^{(\alpha)}, \mathbf{z}_2^{(\beta)} \right)
 \end{aligned} \tag{37}$$

Here, $\overset{*}{\bar{\mathbf{r}}}^{(\beta)}$ denotes the rate of change of the position vector for a point on the surface of ellipsoid β that remains in contact with the given material point $P^{(\alpha)}$. Persistent contact between the material point $P^{(\alpha)}$ and the boundary of body β is characterized by the conditions

$$d^{(\alpha\beta)} = 0 \quad , \quad \dot{d}^{(\alpha\beta)} = 0 \tag{38}$$

It has been shown elsewhere [28] that it is impossible for a homogeneously deforming elastic body (hence, also a Cosserat point of the type used here) to enter into a state of *persistent* contact while preserving its total energy. However, persistent contact can be assumed by approximation when a limited amount of penetration is allowed (*i.e.*, when $d^{(\alpha\beta)} \leq 0$ and

$\dot{d}^{(\alpha\beta)} \doteq 0$), as is the case when the contact constraints are enforced by a penalty method. In this case, the preceding constraint conditions yield (generalized) contact forces, such that the original equations of motion (24) for each of the two bodies become

$$\begin{aligned}\dot{\mathbf{z}}_1^{(\alpha)} &= \mathbf{z}_2^{(\alpha)} + \mathbf{c}_1^{(\alpha)} \\ \dot{\mathbf{z}}_2^{(\alpha)} &= \mathbf{h}^{(\alpha)} + \left(\mathbf{M}^{(\alpha)}\right)^{-1} \mathbf{c}_2^{(\alpha)}\end{aligned}\quad (39)$$

The quantities $\mathbf{c}_1^{(\alpha)}$ and $\mathbf{c}_2^{(\alpha)}$, $\alpha = 1, 2$ are (generalized) contact forces and are determined from (36) and (37) using the Lagrange multiplier method as

$$\mathbf{c}_1^{(\alpha)} = \gamma_1^{(\alpha)} \frac{\partial \tilde{\phi}_1}{\partial \mathbf{z}_1^{(\alpha)}} \quad , \quad \mathbf{c}_2^{(\alpha)} = \gamma_2^{(\alpha)} \frac{\partial \tilde{\phi}_2}{\partial \mathbf{z}_2^{(\alpha)}}\quad (40)$$

Here, the scalars γ_1 and γ_2 are Lagrange multipliers associated with the constraints on $\tilde{\phi}_1$ and $\tilde{\phi}_2$, respectively, and are determined numerically by a process described in Section 4.1. In general, a body may be in contact with more than one bodies at the same time. Naturally, the total constraint forces applied to a particular body are determined by accounting for all active contact pairs involving that body.

3. Implementation of the Cosserat point model

3.1 Time integration algorithm

In this work, a simple explicit predictor-corrector integration scheme [29] is employed based on the forward Cauchy-Euler method. The proposed integration scheme for equations (39) is outlined here for the case of contact between a pair of Cosserat points. The corresponding schemes for the unconstrained equations (24), as well as for the case of multiple contacts can be easily deduced. Suppressing, for notational simplicity, the body index, the discrete counterpart of (39) is written as

$$\begin{aligned}\tilde{\mathbf{z}}_{1,k+1} &= \mathbf{z}_{1,k} + \Delta t \mathbf{z}_{2,k} \text{ ,} \\ \gamma_{1,k+1} &= \gamma_{1,k} + p_1 \phi_1(\tilde{\mathbf{z}}_{1,k+1}) \text{ ,} \\ \gamma_{2,k+1} &= \gamma_{2,k} + p_2 \phi_2(\tilde{\mathbf{z}}_{1,k+1}, \mathbf{z}_{2,k}) \text{ ,} \\ \mathbf{z}_{1,k+1} &= \tilde{\mathbf{z}}_{1,k+1} + \Delta t \mathbf{c}_1(\gamma_{1,k+1}, \tilde{\mathbf{z}}_{1,k+1}) \text{ ,} \\ \mathbf{z}_{2,k+1} &= \tilde{\mathbf{z}}_{2,k} + \Delta t \left[\mathbf{h}(\tilde{\mathbf{z}}_{1,k+1}) + \mathbf{M}^{-1} \mathbf{c}_2(\gamma_{2,k+1}, \tilde{\mathbf{z}}_{1,k+1}, \mathbf{z}_{2,k}) \right]\end{aligned}\quad (41)$$

where Δt is the stepsize and $(\)_k$ denotes the numerical approximations of $(\)$ at time $t = t_k$. Equation (41)₁ uses the forward Cauchy-Euler method to compute a predictor $\tilde{\mathbf{z}}_{1,k+1}$ to the generalized position $\mathbf{z}_{1,k+1}$. The detection of contact, the determination of contact points, the computation of contact forces \mathbf{c}_1 , \mathbf{c}_2 and constraint functions ϕ_1 , ϕ_2 are all based on this predictor value. Also, equations (41)_{2,3} compute approximations to the Lagrange multipliers of equation (40) by penalizing the constraint functions ϕ_1 and ϕ_2 , respectively. To limit penetration, the penalty parameter p_1 is chosen to depend on of the Young's moduli of the contacting Cosserat points. On the other hand, the parameter p_2 is deduced from the

requirement that the total system energy be conserved at each time step, see Section 4.2. Equations (41)_{4,5} employ again the forward Cauchy-Euler integration method for (39). When a Cosserat point is not in contact, then clearly $\mathbf{c}_1 = \mathbf{c}_2 = 0$ and $\gamma_1 = \gamma_2 = 0$. The latter serve as initial conditions for (41)_{2,3} whenever contact is initiated.

A simple adaptive time-stepping scheme is implemented, such that the initial user-specified stepsize Δt is sharply reduced when the state $\tilde{\mathbf{z}}_{1,k+1}$ predicts contact between Cosserat points. This is done to limit penetration and control the total system energy. However, the reduction in stepsize is capped by a user-specified lower-bound in order to safeguard against excessive computational cost. As long as contact persists, time integration continues with the fixed stepsize. Once contact is lost, the Lagrange multipliers γ_1 and γ_2 are reset to zero and the stepsize is gradually increased back to its initial value.

3.2 Energy conservation

The total energy E of a Cosserat point, as modeled in Section 2.2, is comprised of the kinetic energy T , the strain energy S and the gravitational potential energy U , namely

$$E = T + S + U \quad (42)$$

Recalling equations (16) and (23-25), the three energies take the form

$$T = \frac{1}{2} \mathbf{z}_2 \cdot (\mathbf{M} \mathbf{z}_2) \quad (43)$$

$$S = m\psi = \frac{V}{2} \left[\lambda (\text{tr} E)^2 + 2\mu E \cdot E \right] \quad (44)$$

and

$$U = -\mathbf{q} \cdot \mathbf{z}_1 \quad (45)$$

In this formulation, the effects of friction during dynamic contact between Cosserat points or between a Cosserat point and a fixed boundary are neglected. Assuming, further, that contact is ideally elastic, it follows that the total system energy E^s is a conserved quantity. Hence, in the discrete setting of Section 4.1, one needs to approximately enforce the condition

$$E_{k+1}^s = E_k^s \quad (46)$$

where E_{k+1}^s and E_k^s denote the total system energy at time t_{k+1} and t_k , respectively. Recalling (42), it follows that equation (46) can be rewritten as

$$T_{k+1}^s + S_{k+1}^s + U_{k+1}^s = E_k^s \quad (47)$$

where T_{k+1}^s , S_{k+1}^s and U_{k+1}^s respectively denote the total kinetic energy, total strain energy and total gravitational potential energy of the system at time t_{k+1} . With reference to the time integration scheme (41), it is clear that, once the generalized position vector $_{1,k+1}$ of each Cosserat point is determined using equations (41)_{1,4}, the strain energy and the gravitational potential of each point at time t_{k+1} can be computed directly from equations (44) and (45), respectively. Upon focusing only on a pair (α, β) of contacting Cosserat points, equation (46) reduces to

$$\sum_{i=\alpha,\beta} \frac{1}{2} \mathbf{z}_{2,k+1}^{(i)} \cdot (\mathbf{M}^{(i)} \mathbf{z}_{2,k+1}^{(i)}) = \sum_{i=\alpha,\beta} [E_k^{(i)} - S_{k+1}^{(i)} - U_{k+1}^{(i)}] \quad (48)$$

where all the terms on the right-hand side of the preceding equation are known. The generalized velocity \mathbf{z}_2 is updated using (41)₅, where the unknown quantities are the velocity constraint forces $\mathbf{c}_{2,k+1}$ computed from (40)₂ and (41)₃. Since the relative normal velocity function ϕ_2 in (41)₃ is determined from given position vectors $\tilde{\mathbf{z}}_{1,k+1}$ and $\mathbf{z}_{2,k}$, the only unknown quantity is the parameter p_2 , which is computed from (48). Given the explicit time integration, multiple simultaneous impacts of a Cosserat point are handled trivially. In all, equation (48) is enforced for all pairs of contacting Cosserat points, which leads to the conservation of the total system energy to within the deviations due to the truncation error of the discrete time integration scheme.

4. Numerical simulations

The numerical simulations contained in this section have been carried out to test the broad predictive capabilities of the Cosserat point model and the computational efficiency of the algorithmic implementation. The latter is achieved by employing object-oriented programming, see [30] for a complete description. In all simulations, the elastic material parameters of each body are $\lambda = 3.46[\text{MPa}]$, $\mu = 2.31[\text{MPa}]$, and the mass density is $\rho = 7850[\text{kg/m}^3]$. Also, the initial and maximal stepsize is $5.0 \times 10^{-5}[\text{s}]$, while the minimal stepsize is $1.0 \times 10^{-5}[\text{s}]$. Finally, $p_1 = 2 \times 10^4$ for contact between Cosserat points and $p_1 = 2 \times 10^5$ for contact between a Cosserat point and the rigid hopper wall.

4.1 A particle wave problem

The purpose of this elementary example is to test the ability of the contact detection scheme to correctly determine the positions of contact points and directions of contact forces. Here, five Cosserat points are traveling on the same straight line in the absence of gravitational force. The first point has initial velocity of $1[\text{m/s}]$, while the remaining points have initial velocity of $3[\text{m/s}]$. The points are associated with identical ellipsoidal reference configurations with lengths of the principal semi-axes of $0.1[\text{m}]$ and $0.05[\text{m}]$ transversely to the motion and $0.06[\text{m}]$ in the direction of the motion. It is clear that the only external forces acting on each ellipsoid are due to dynamic contacts. The initial stages of the “chain reaction” of collisions triggered by the slower first point is depicted in Fig. 6. The locus of mass centers of each body versus time are plotted in Fig. 7. This figure shows that all five ellipsoids move along a straight path to within negligible numerical error, as expected.

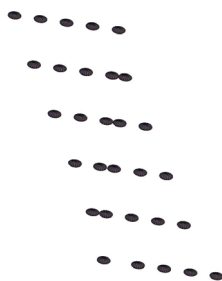


Fig. 6. Particle wave problem: Consecutive collisions in a chain reaction.

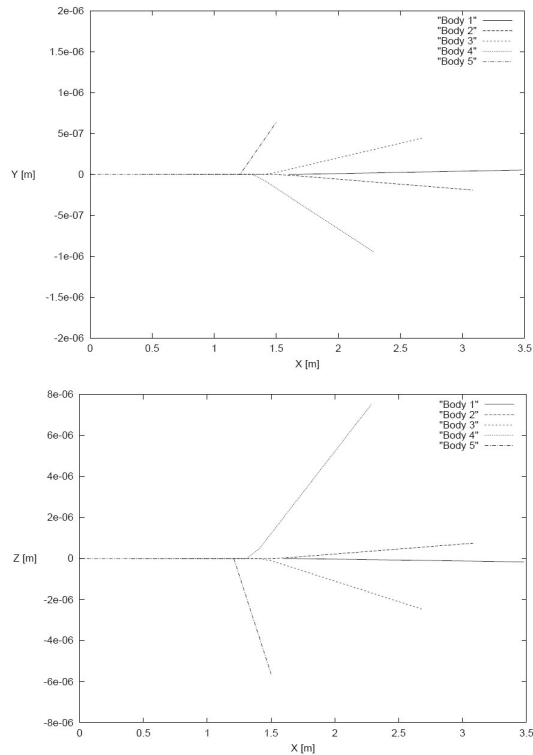


Fig. 7. Particle wave problem: Projections of the paths of the five Cosserat points in X-Y and X-Z plane.

5.1 Particulate flow through a stationary hopper

The flow of a large volume of particulate material through chutes [31], hoppers [32,33], and pipes [34,35] is of great interest in process engineering. In this simulation, 1008 stationary Cosserat points are placed in a $14 \times 12 \times 6$ cubic array on the top part of a cone-shaped hopper and subsequently are allowed to flow under gravity past the lower opening section of the hopper, as shown in Figures 8 -10. All particles are modeled as Cosserat points having a spherical reference configuration with radius 0.05[m]. The initial distance between the centers of neighboring spheres on layers parallel to the cubic phases is set to 0.13[m]. Also, the elevation of the spheres at the bottom layer of the cubic array is 1.2[m] above the lower opening section. The hopper is a conical section with rigid and fixed lateral surface. The height of the hopper is 2.5[m], and the diameters of the lower and upper opening circular holes are 1.2[m] and 3.7[m], respectively.

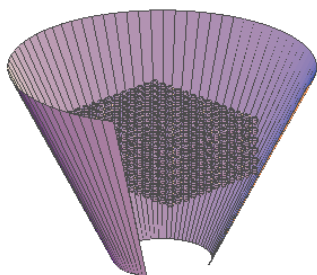


Fig. 8. Flow through a stationary hopper: Reference configuration at time $t=0.0[s]$.

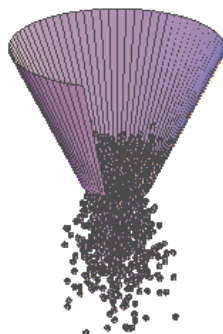


Fig. 9. Flow through a stationary hopper: Configuration at time $t=0.66[s]$.



Fig. 10. Flow through a stationary hopper: Configuration at time $t=1.2[s]$.

Figure 11 shows the number of contacts between Cosserat points as a function of time. Clearly, this number reaches a peak when most of the particles pass through the lower opening section of the hopper. The dependence of the run-time per step on the number of contacts is shown in Fig. 12. Note that the run-time per step is essentially independent of the number of contacts (on the other hand, the stepsize *does* depend on this number!). The total energy of the Cosserat points in the hopper flow simulation is plotted in Fig. 13 and is conserved with high accuracy. The degree of deviation from exact energy conservation can be appreciated in Fig. 14. Indeed, it is clear that energy is very accurately conserved during the time interval $[0.15, 0.7]$ where most contacts occurs. This is precisely the interval in which both the stepsize is reduced and the energy conservation scheme of Section 4.2 is massively employed. On the other hand, both at the very beginning (when contacts have not been initiated) and toward the end of the simulation (when the particles scatter) the energy shows small fluctuations due to the fact that the smooth time integration algorithm (*i.e.*, without contact) is not energy-conserving.

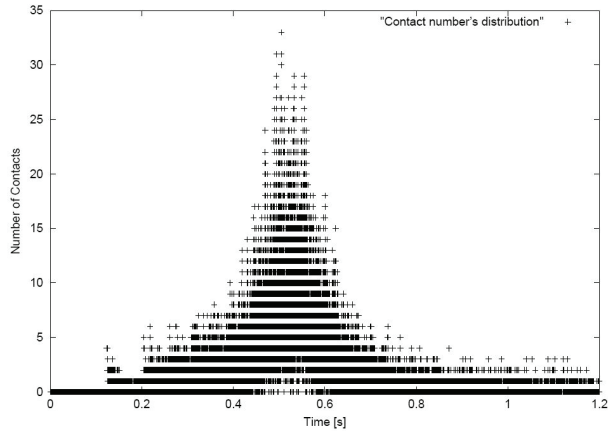


Fig. 11. Flow through a stationary hopper: Number of contact as a function of time.

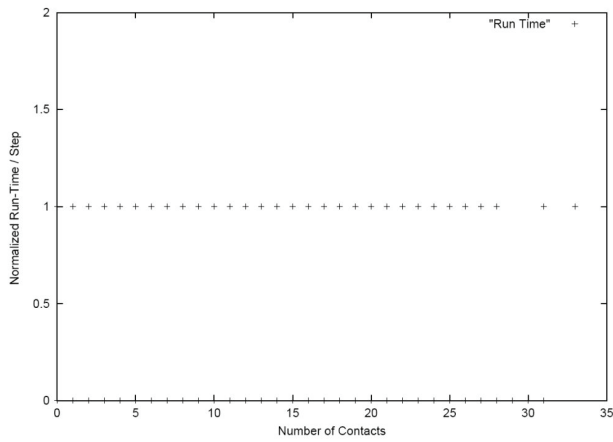


Fig. 12. Flow through a stationary hopper: Normalized run-time per step as a function of the number of contacts.

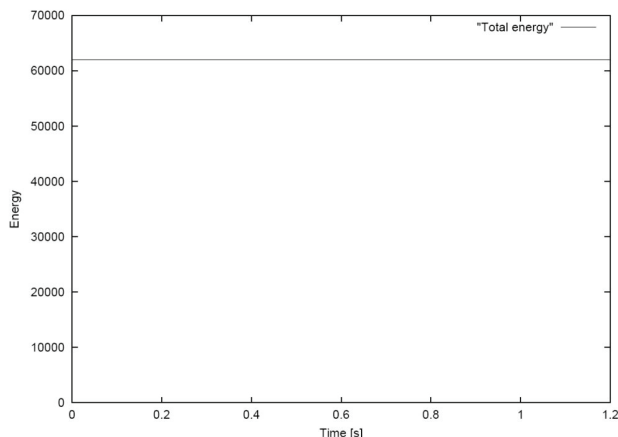


Fig. 13. Flow through a stationary hopper: Total system energy as a function of time.

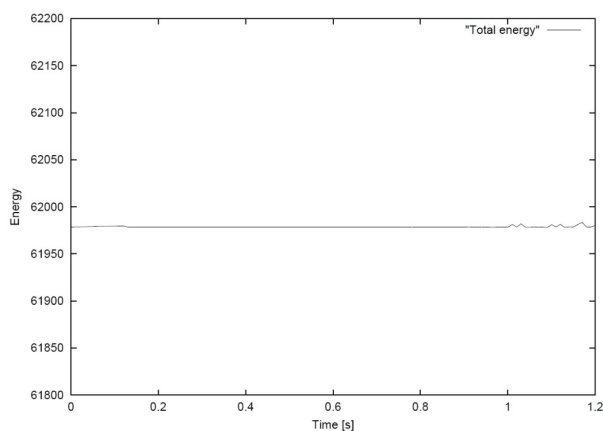


Fig. 14. Flow through a stationary hopper: Total system energy as a function of time (zoom on small energy fluctuations).

A series of hopper flow simulations with varying number of particles is conducted to assess the scalability of the implementation. In addition to the preceding one involving 1,008 particles in a $14 \times 12 \times 6$ cubic array, simulations are also run with 2,016 particles ($14 \times 12 \times 12$), 10,200 particles ($30 \times 20 \times 17$), 20,400 particles ($30 \times 20 \times 34$), and 40,320 particles ($28 \times 40 \times 36$). The geometric properties of the hopper are as described earlier, while the elevation of the bottom layer of particles is 1.13[m] above the lower opening of the hopper for the first four simulations and 1.44[m] for the last one. To render the scaling more meaningful, the spheres are taken to have radius 0.05[m] in the first two and 0.025[m] in the last three simulations. Correspondingly, the distances between the centers of the spheres on layers parallel to the faces of the cubic array are taken to be 0.13[m] for the first two and 0.065[m] for the last three simulations. Figures 15 and 16 show the total run-time per time-step and the total memory allocation as a function of the number of particles, as obtained on a commodity-type personal computer (Pentium IV, 1.4 GHz; 512 MB RAM) using the GNU C++ compiler. It is clear from these figures that the memory scales linearly with the number of particles, while the run-time scales super-linearly with scaling exponent approximately equal to 1.6.

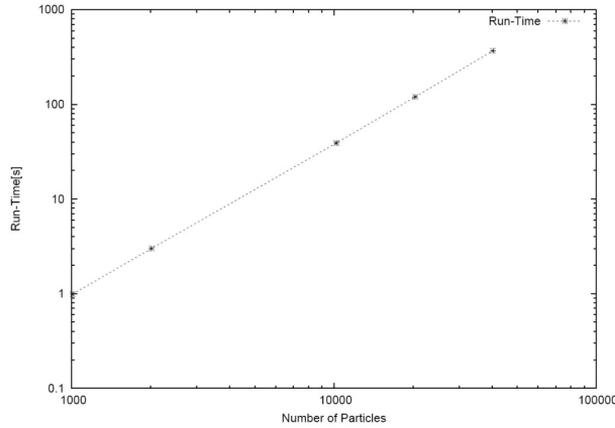


Fig. 15. Flow through a stationary hopper: Run-time as a function of the number of particles.

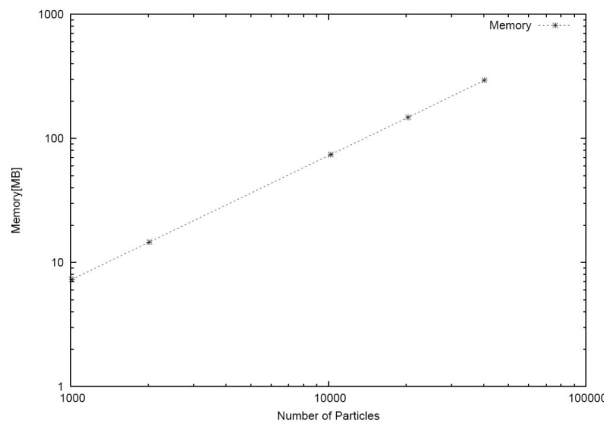


Fig. 16. Flow through a stationary hopper: Total memory allocation as a function of the number of particles.

4.2 Particulate flow through a horizontally vibrating hopper

This example is used to model the flow of a granular medium in a hopper that vibrates horizontally. Vibration is widely used in various industrial operations for smooth discharge of particles from a hopper [36]. In this simulation, a $14 \times 6 \times 6$ cubic array of 504 Cosserat points of spherical reference configuration flows under gravity through the vibrating hopper. All pertinent dimensions for the hopper and the spheres are identical to those of the initial problem in Section 5.2. In addition, the vibration of the hopper is sinusoidal and takes place in the direction of the "long" side of the cubic array with amplitude $A = 0.2[\text{m}]$ and frequency $f = 0.5[\text{Hz}]$. Figures 17 - 20 show a view of the system at different times, as projected on the plane of vibration.

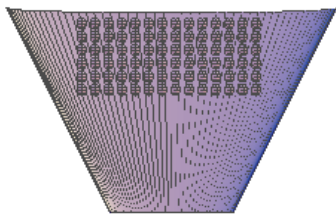


Fig. 17. Flow through a vibrating hopper:
Configuration at time $t=0.0[s]$.

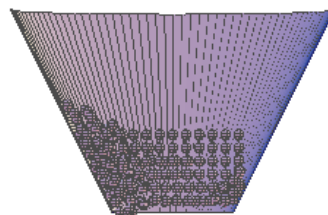


Fig. 18. Flow through a vibrating hopper:
Configuration at time $t=0.51[s]$.

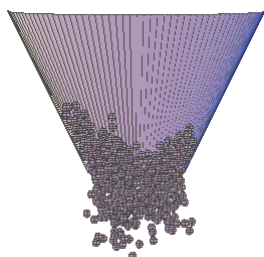


Fig. 19. Flow through a vibrating hopper:
Configuration at time $t=0.63[s]$.

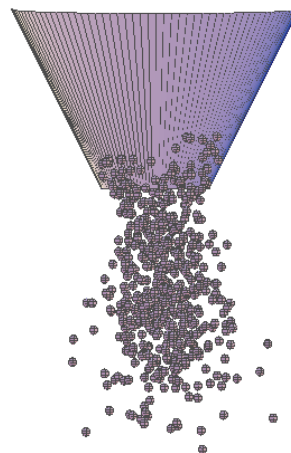


Fig. 20. Flow through a vibrating hopper:
Configuration at time $t=0.82[s]$.

Closure

The theory of Cosserat points is employed to develop a simple model that can be used for frictionless dynamic contact involving large numbers of particulates of ellipsoidal shape. A simple, yet robust, algorithm is proposed to enforce the impenetrability constraint and conserve energy during the impact events. An object-oriented implementation allows for the effective management of the data and yields reasonable scalability results. Overall, the Cosserat point formalism permits the incorporation of limited deformability in the particles, which one seeks a balance between accuracy and computational tractability.

References

- [1] M.B. Rubin. On the theory of a Cosserat point and its application to the numerical solution of continuum problems. *ASME Journal of Applied Mechanics*, 52:368–372, 1985.
- [2] A.E. Green and P.M. Naghdi. A thermomechanical theory of a Cosserat point with application to composite materials. *Quarterly Journal of Mechanics and Applied Mathematics*, 44:335–355, 1991.
- [3] S.S. Antman. The theory of rods. In S. Flügge, editor, *Handbuch der Physik VIa/2*, pages 641–703. Springer-Verlag, Berlin, 1972.
- [4] P.M. Naghdi. The theory of shells and plates. In S. Flügge, editor, *Handbuch der Physik VIa/2*, pages 425–640. Springer-Verlag, Berlin, 1972.
- [5] C. Woźniak. Basic concepts of the theory of discrete elasticity. *Bull. Acad. Pol. Sci.*, 19:753–758, 1971.
- [6] C. Woźniak. Discrete elastic Cosserat media. *Archives of Mechanics*, 25:119–136, 1973.
- [7] J.J. Slawianowski. Analytical mechanics of finite homogeneous strains. *Archives of Mechanics*, 26:569–587, 1974.
- [8] J.J. Slawianowski. Newtonian dynamics of homogeneous strains. *Archives of Mechanics*, 27:93–102, 1975.
- [9] H. Cohen and R.G. Muncaster. *The Theory of Pseudo-rigid Bodies*. Springer-Verlag, New York, 1988.
- [10] M.B. Rubin. Free vibration of a rectangular parallelepiped using the theory of a Cosserat point. *ASME Journal of Applied Mechanics*, 53:45–50, 1986.
- [11] P.C. Varadi, G.-J. Lo, O. M. O'Reilly, and P. Papadopoulos. A novel approach to vehicle dynamics using the theory of a Cosserat point and its application to collision analyses of platooning vehicles. *Vehicle Systems Dynamics*, 32:85–108, 1999.
- [12] M.B. Rubin. Numerical solution procedures for nonlinear elastic rods using the theory of a Cosserat point. *International Journal of Solids and Structures*, 38:4395–4437, 2001.
- [13] O.M. O'Reilly. A properly invariant theory of infinitesimal deformations of an elastic Cosserat point. *Journal of Applied Mathematics and Physics (ZAMP)*, 47:179–193, 1996.
- [14] A. Munjizk and K.R.F. Andrews. NBS contact detection algorithm for bodies of similar size. *International Journal of Numerical Methods in Engineering*, 43:131–149, 1998.
- [15] T.-T. Ng. Numerical simulations of granular soil using elliptical particles. *Computers and Geotechnics*, 16:153–169, 1994. 18 Version: December 12, 2007, 08:25 G.-J. Lo and P. Papadopoulos
- [16] J.M. Ting, M. Khwaja, L.R. Meachum, and J.D. Rowell. An ellipse-based discrete element model for granular materials. *International Journal for Numerical and Analytical Methods in Geomechanics*, 17:603–623, 1993.
- [17] D.S. Preece and S.L. Burchell. Variation of spherical element packing angle and its influence on computer simulations of blasted induced rock motion. *Proceedings of 2nd U.S. Conference on Discrete Element Methods*, 1993.
- [18] C.-W. Hong. New concept for simulating particle packing in colloidal forming processes. *Journal of the American Ceramic Society*, 80(10):2517–2524, 1997.

- [19] J.R. Williams and A. Pentland. Superquadrics and model dynamics for discrete elements in interactive design. *Journal of Computer Aided Engineering – Engineering Computations*, 9(2), 1992.
- [20] C. Truesdell and R.A. Toupin. Principles of classical mechanics and field theory. In S. Flügge, editor, *Handbuch der Physik*, volume III/1. Springer-Verlag, Berlin, 1960.
- [21] O.M. O'Reilly, P. Papadopoulos, G.-J. Lo, and P.C. Varadi. Models of vehicular collision: development and simulation with emphasis on safety V: Medusa: theory, examples, user's manual, programmer's guide and code. California PATH research report UCB-ITS-PRR-99-32, U. C. Berkeley, 1999.
- [22] J.R. Williams and R. O'Connor. A linear complexity intersection algorithm for discrete element simulation of arbitrary geometries. *Engineering Computations*, 12:185–201, 1995.
- [23] J. Kowalik and M.R. Osborne. *Methods for Unconstrained Optimization Problems*. American Elsevier Publishing Company, New York, 1968.
- [24] D.G. Luenberger. *Linear and Nonlinear Programming*. Addison-Wesley, Reading, 2nd edition, 1984.
- [25] W.H. Press, S.A. Teukolsky, W.T. Vetterling, and B.P. Flannery. *Numerical Recipes in C: the Art of Scientific Computing*. Cambridge University Press, 4th edition, 1992.
- [26] J. Casey. Geometrical derivation of Lagrange's equations for a system of particles. *American Journal of Physics*, 62:836–847, 1994.
- [27] J. Casey. On the advantages of a geometrical viewpoint in the derivation of Lagrange's equations for a rigid continuum. *Journal of Applied Mathematics and Physics (ZAMP)*, 46(Special Issue):805–847, 1995.
- [28] J.M. Solberg and P. Papadopoulos. Impact of an elastic pseudo-rigid body on a rigid foundation. *Int. J. Engr. Sci.*, 38:589–603, 2000.
- [29] T. Belytschko and T.J.R. Hughes. *Computational Methods for Transient Analysis*. North-Holland, New York, 1983.
- [30] G.-J. Lo. A Large-Scale Discrete Element Contact/Impact Simulation using Object-Oriented Programming. PhD thesis, University of California, Berkeley, 2000.19 Version: December 12, 2007, 08:25 Dynamic contact between Cosserat points
- [31] L. Vu-Quoc and Z. Xiang. An accurate and efficient tangential force-displacement model for elastic frictional contact in particle-flow simulations. *Mechanics of Materials*, 31:235–269, 1999.
- [32] A.V. Potapov and C.S. Campbell. Computer simulation of hopper flow. *Physics of Fluids*, 8:2884–2894, 1996.
- [33] C. Thornton. Applications of DEM to process engineering problems. *Engineering Computations*, 9:289–297, 1992.
- [34] O. Moriyama, T. Isoda, N. Kuroiwa, M. Kanda, et al. Dynamics of granular flow through a vertical pipe: effect of medium flow. *Journal of the Physical Society of Japan*, 67:1616–1625, 1998.
- [35] J.-L. Aider, N. Sommer, T. Raafat, and J.-P. Hulin. Experimental study of a granular flow in a vertical pipe: A spatiotemporal analysis. *Physical Review E*, 59:778–786, 1999.
- [36] R.C. Weathers, M.L. Hunt, C.E. Brennen, A.T. Lee, and C.R. Wassgren. Effects of horizontal vibration on hopper flows of granular materials. *Physics of Fluids*, 11:68–75, 1999.